POLITECNICO DI TORINO
Repository ISTITUZIONALE

Overprinting with tomographic volumetric additive manufacturing

*Original*
Overprinting with tomographic volumetric additive manufacturing / Wechsler, F., Sgarminato, V., Rizzo, R., Nicolet, B., Jakob, W., Moser, C.. - In: NATURE COMMUNICATIONS. - ISSN 2041-1723. - 17:1(2026). [10.1038/s41467-026-73477-3]

*Availability:*
This version is available at: 11583/3015172 since: 2026-09-04T13:48:19Z

*Publisher:*
Nature Research

*Published*
DOI:10.1038/s41467-026-73477-3

*Terms of use:*

This article is made available under terms and conditions as specified in the corresponding bibliographic description in the repository

*Publisher copyright*

(Article begins on next page)

19 November 2026

nature communications

Article

https://doi.org/10.1038/s41467-026-73477-3

# Overprinting with tomographic volumetric additive manufacturing

Received: 18 July 2025

Accepted: 8 May 2026

Published online: 08 June 2026

Check for updates

Felix Wechsler[1], Viola Sgarminato[1,2], Riccardo Rizzo[1], Baptiste Nicolet[3,4], Wenzel Jakob[3] & Christophe Moser[1]

Tomographic Volumetric Additive Manufacturing (TVAM) is a light-based 3D printing technique capable of producing centimeter-scale objects within seconds. A key challenge lies in the calculation of tomographic projection patterns under non-standard conditions, such as the presence of occlusions and materials with diverse optical properties, including varying refractive indices or scattering surfaces.

This work demonstrates a broad range of overprinting scenarios, where new structures are directly printed onto or around pre-existing components made from different materials. Our simulations and experimental verifications perform overprinting of absorbing, refracting, reflecting and scattering elements in both round and square vials.

All scenarios are optimized with our differentiable, physically based ray-optics approach using the open-source Dr.TVAM framework, delivering high-quality projections for both laser- and LED-based illuminations within minutes and lower-quality projections within seconds, exceeding existing open-source solutions in speed, flexibility, and quality.

Tomographic volumetric additive manufacturing (TVAM)[1–3] is a rapid light-based 3D printing technique that enables manufacturing of centimeter-scale structures in seconds. Pre-calculated 2D patterns are projected onto a rotating vial filled with a photosensitive (single-photon absorption) resin. The patterns propagate into the resin and deposit a 3D energy dose over time. Once the accumulated energy dose exceeds a threshold, local network formation occurs[4].

Due to the similarity between TVAM and computed tomography (CT), the Radon transform and its adjoint (the backprojection) can be employed as a physical forward model for light propagation. However, these models neglect the intensity loss of light as it propagates through the medium, making the attenuated Radon transform a more appropriate model[1,5]. In the early stages, light patterns for TVAM were calculated using filtered backprojection. However, this approach resulted in physically impossible negative projection intensities. While these values are easily clipped to zero, doing so leads to an energy mismatch that causes serious artifacts into the final prints. Rackson et al.[6] utilised the thresholding behaviour to develop an iterative algorithm that ensures object regions receive more dose than an upper threshold while void regions remain below a lower threshold. This concept was transformed into a loss function that was then optimized using a gradient descent-based optimiser[7,8]. A more generalised version of a similar loss function has been introduced by Li et al.[9].

Moreover, the rotating vial was initially placed in an index-matching bath to approximately eliminate light refractions at the air-to-vial-to-resin interfaces. Later, this limitation was addressed by correcting the patterns for refraction [10,11], allowing vials to be used in air. However, this post-processing is only an approximation, as it cannot be accurately combined with the correct attenuation of the rays within the vial. Consequently, more powerful frameworks based on ray tracing schemes have been proposed[12,13]. In these works, rays are traced through a voxel grid, allowing for correct energy deposition and refraction accounting.

[1]Laboratory of Applied Photonics Devices, École polytechnique fédérale de Lausanne (EPFL), Lausanne, Switzerland. [2]BIOINSIDE Lab, Department of Mechanical and Aerospace Engineering, Politecnico di Torino, Italy. [3]Realistic Graphics Lab, École polytechnique fédérale de Lausanne (EPFL), Lausanne, Switzerland. [4]NVIDIA, Zürich, Switzerland. e-mail: overprinting@felixwechsler.science; wenzel.jakob@epfl.ch; christophe.moser@epfl.ch

TVAM has proven to be extremely flexible and has been utilised for a wide range of materials and printing scenarios[14]. Particularly, modeling light scattering has been successful in printing in media with scattering particles[13], such as bio-resins[15]. Early TVAM setups employed laser diodes (referred to as LaserTVAM), which resulted in striation artifacts[16,17]. By using LED illumination for TVAM (LEDTVAM), these striations were largely mitigated, enabling the production of optical elements with smooth surfaces [18]. As the chemical interactions affect the final print, previous work modeled the physical and chemical processes of TVAM[19] and corrected for effects such as diffusion of inhibitors[20]. Also holographic projection schemes with digital micromirror devices have been used to increase the laser light engine efficiency[21].

Due to the rotation of the vial the printing projector has access to different sides of existing structures. Hence, overprinting of preexisting structures has emerged as a potential application of TVAM. Indeed, other 3D printing techniques are often limited because they build the 3D structure from one side and therefore cannot print effectively around occlusions. This capability has been demonstrated in the printing of a handle on a metal screwdriver[1]. However, this work assumed the metal rod to be fully absorptive, which is not appropriate for many surfaces. Later, more complex geometries were overprinted over existing structures[22], although in this work the existing structure was completely disregarded in the pattern optimisation. Similarly, a gelatin methacrylate (Gel-MA) hydrogel was successfully overprinted over an endoskeletal system[23].

Recently, a more complex method called GRACE (Generative, Adaptive, Context-Aware 3D Printing)[24] was introduced. Using a light sheet imaging system, the authors detected spheres and overprinted connected channels over these structures. However, the light transport model still seems to be limited to fully transparent or fully blocking occlusions.

In recent years, several studies have demonstrated the potential of TVAM as a bioprinting technique capable of fabricating cellularized constructs with diverse geometries, sizes, and internal cavities that closely mimic human physiology[2,25]. Indeed, TVAM is particularly well-suited for printing hollow 3D structures, as it does not require sacrificial support materials. The integration of bioprinting with microfluidics has gained increasing attention, as it enables the fabrication of anatomically relevant 2.5D and 3D structures within dynamic and physiologically realistic environments[26]. For example, TVAM has also been explored for the fabrication of perfusable constructs with potential for microfluidic systems and organ-on-chip[27,28]. However, efforts to date have revolved around standard, multi-step processes that include printing in round vials, recovering and post-processing of the printed object, and finally assembly of the multicomponent microfluidic chamber. In addition to being tedious and inefficient, this procedure significantly increases the risk of leakage and contamination. Similar issues are intrinsic to alternative approaches such as embedded printing and digital light processing.

Recently, Nicolet et al.[13] introduced a physically-based differentiable simulation software for TVAM, named Dr.TVAM, built on the open-source differentiable renderer Mitsuba 3[29]. Since it is based on a general rendering system, Dr.TVAM enables integration of other components or occlusions in the printing vial, and supports customizable printing geometries. Its physically-based optical simulation of the TVAM process allows to account for various effects such as scattering, absorption, arbitrary reflections and refractions.

In this work we introduce overprinting scenarios and highlight the versatility of our framework Dr. TVAM across various contexts and applications. Our simulations and experiments build on the versatility of this platform for pattern optimisation.

First, we lay the foundation for a new, streamlined workflow of the biofabrication of microfluidic chips. By accounting for unconventional vial geometry (square cuvette) and occluding elements (inlets and outlets), Dr.TVAM enables overprinting of microfluidic networks into preassembled 3D chips, thus opening to a new generation of on-chip technologies. Based on this workflow, we also overprinted small glass spheres at arbitrary locations by detecting them and hereby showing context-aware fabrication of microfluidic chips. Next, we print a simple gear on a reflective rod and demonstrate that more complex light modeling outperforms existing solutions. Finally, we overprint a mini projector on a LED. Furthermore, its ability to handle non-telecentric configurations makes Dr.TVAM, to the best of our knowledge, the only open-source available software for the simulation and optimisation of LED-based TVAM systems.

All source code, 3D meshes and configuration scripts are released for reproducibility.

## Results

### Perfusion system for bio-applications

To demonstrate the capability of Dr.TVAM in fabricating microfluidic chips within flat, imaging-compatible vials using a biocompatible resin, we designed a custom platform. This platform consists of a transparent chamber made from a cut 1 cm polystyrene square-shaped cuvette (see Fig. 1). Stereolithography (SLA)-printed adapters featuring inlets, outlets, barbed connectors for tubing, and circular supports for mounting to a rotational stage were press-fitted onto both ends, creating a leak-proof system. The widely used biocompatible photopolymer gelatin methacryloyl (Gel-MA) with LAP as the photoinitiator was used for printing (see Biocompatible resin for details).

In this overprinting scenario, the adapters were fabricated from black resin, so the inlet and outlet occlusions were assumed to be fully light-absorbing. Various perfusable models, including a simple straight channel, a spiral, and a branched geometry, were optimized using Dr.TVAM, accounting for the square container and the presence of these occluding elements. In TVAM typically round vials are used to contain the resin but since our framework is very general, arbitrary container shapes are possible. This experiment was performed with the laser-based TVAM setup (LaserTVAM) described in Section LaserTVAM. A schematic of the LaserTVAM setup is shown in Fig. 1a. The optimisation results are shown in Fig. 1b, c, which display the dose histogram and a slice of the final dose distribution after projection of the patterns, respectively.

The histogram plots the voxel intensities for both object and void regions. Note that the voxel count is on a logarithmic scale. Histograms plots are an effective way to judge if there is a good separation between void and object exposure[6]. Although the dose in Fig. 1c is not perfectly homogeneous, applying a threshold (indicated by a dashed red line in the histogram) yields a best Intersection over Union (IoU) score of 0.9972, which is close to the maximum possible value of 1. Example projection patterns are shown in Fig. 1d–f. For instance, Fig. 1d shows the pattern for a projection angle of 45°. Here, light is refracted through both the left and right sides of the cuvette, highlighting the influence of its square geometry. Furthermore, the optimisation restricts light from passing through the corners of the cuvette, as they are frosted and would cause unwanted scattering.

The final prints for three different target shapes are shown in Fig. 1g–i. The designed channel diameters are 0.95 mm, 0.7 mm and 0.95 mm respectively. Experimentally, we measure (1.15 ± 0.1) mm, (0.5 ± 0.1) mm and (0.6 ± 0.1) mm. The deviations can be explained by over- or underpolymerisation, swelling of the material but also diffusion effects of the dye.

Videos of the perfusion can be found in the supplementing material (Supplementary Movie 1, Supplementary Movie 2, Supplementary Movie 3). This non-curved container geometry simplifies imaging, and when used in pre-assembled chips, as in this case, it also allows for the container to remain sealed post-fabrication, thereby maintaining sterile conditions. In summary, using Dr.TVAM we successfully generated optimized patterns for an unconventional square

https://doi.org/10.1038/s41467-026-73477-3

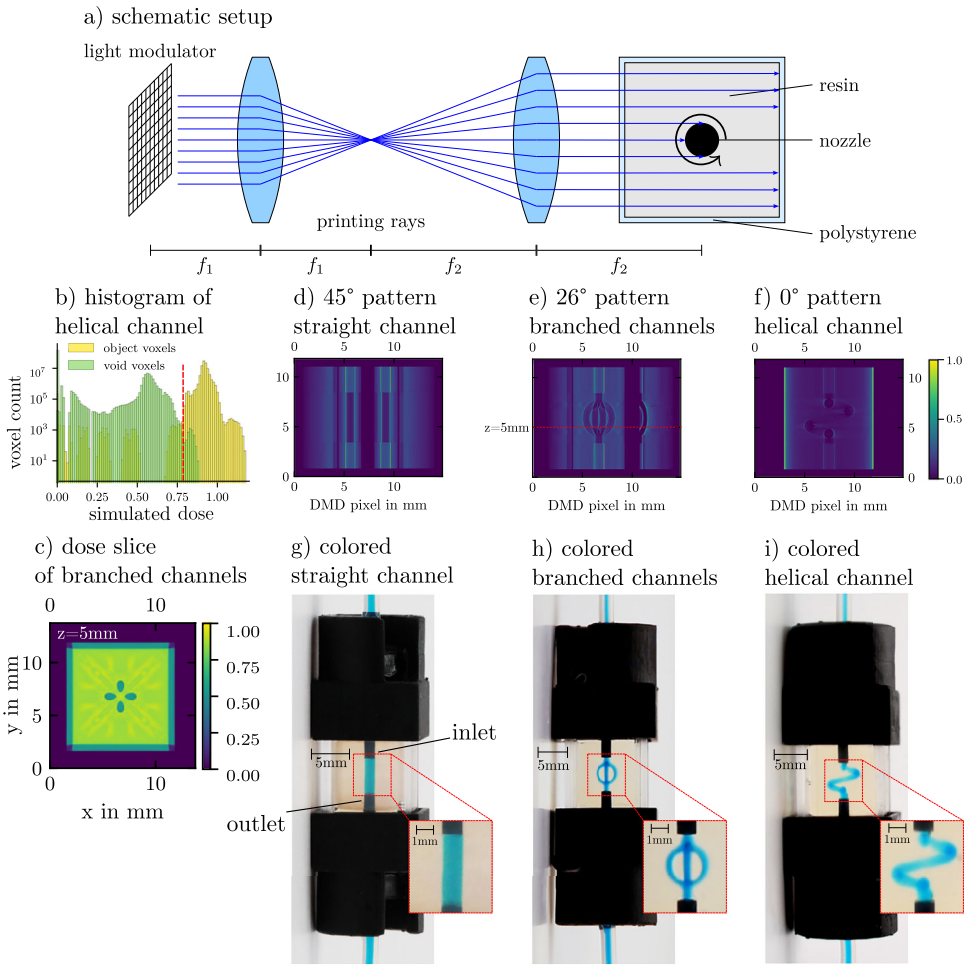



**Fig. 1 | Fabrication of perfusable microfluidic channels in a pre-assembled, square cuvette. a** Schematic setup with projections into a square cuvette. **b** Voxel dose histogram from the simulation. **c** A slice of the cumulative dose map. **d, e, f** Example projection patterns calculated by Dr.TVAM for different angles. The pattern in **d** clearly shows the refractive effect of the square cuvette walls. **g, h, i** Final printed microfluidic channels with different geometries inside the sealed cuvette.

vial geometry with internal occlusions, enabling the fabrication of perfusable microfluidic features within customizable pre-assembled chips.

## Context-aware perfusion system

In this next example, we used the microfluidic chip platform described previously to showcase the capability of Dr.TVAM to rapidly generate projection patterns for case-specific, context-aware printing (Fig. 2).

The process began by filling the square chamber with Gel-MA and positioning two 1 mm glass spheres between the nozzles see Fig. 2a, b. Since Gel-MA is solid at room temperature, we did not observe any movement because of gravity (see also Section Context-aware perfusion system). The spheres possess a different refractive index and refract the light, as indicated in Fig. 2a. A camera-based system captured the coordinates of both spheres from two orthogonal views (0° and 90°), as seen in Fig. 2b. The flat geometry of the cuvette allows for the straightforward determination of the spheres' 3D positions from these two views. By measuring the pixel positions, we extracted the real-world coordinates in under a minute.

Based on these positions, we generated a target geometry and optimized the printing patterns, treating the glass spheres as reflective and refractive occlusions. The quality of the optical simulation was reduced to achieve a fast pattern optimisation time (see details in Section Context-aware perfusion system) of approximately 30 s. The generated patterns defined hollow straight channels (inner diameter 0.7 mm) connecting each sphere to the inlet and outlet of the perfusion system. Additionally, spherical cavities (inner diameter 1.7 mm) were printed around the spheres to secure their position while enabling liquid perfusion. The dose distribution of two different vertical slices in Fig. 2c. Although the dose distribution is not perfectly homogeneous, the highest IoU of 0.9951 indicates successful optimisation. Two example patterns are displayed in Fig. 2d.

To evaluate the performance of the overprinting algorithm, the final print was perfused with a blue food dye solution. As shown in Fig. 2e, this approach enables the rapid fabrication of functional channels around millimetre-scale objects with arbitrary spatial positions within the chamber.

## Gear on metal rod

As previously reported, Kelly et al.[1] successfully printed a handle over an existing metallic screwdriver rod. In their work, however, the metal rod was assumed to be fully light-absorbing. This approximation, while not physically accurate, can be sufficient in specific cases. However, common metal parts like polished steel are highly reflective. In such cases, a significant amount of light is scattered or reflected, which must be taken into account.

To demonstrate our approach experimentally, we printed a gear featuring teeth and circular holes onto a polished steel rod using an acrylate resin (see Section Acrylate for details). A 3D SLA-printed cap was used to position the metal rod in the center of the glass vial. We

https://doi.org/10.1038/s41467-026-73477-3

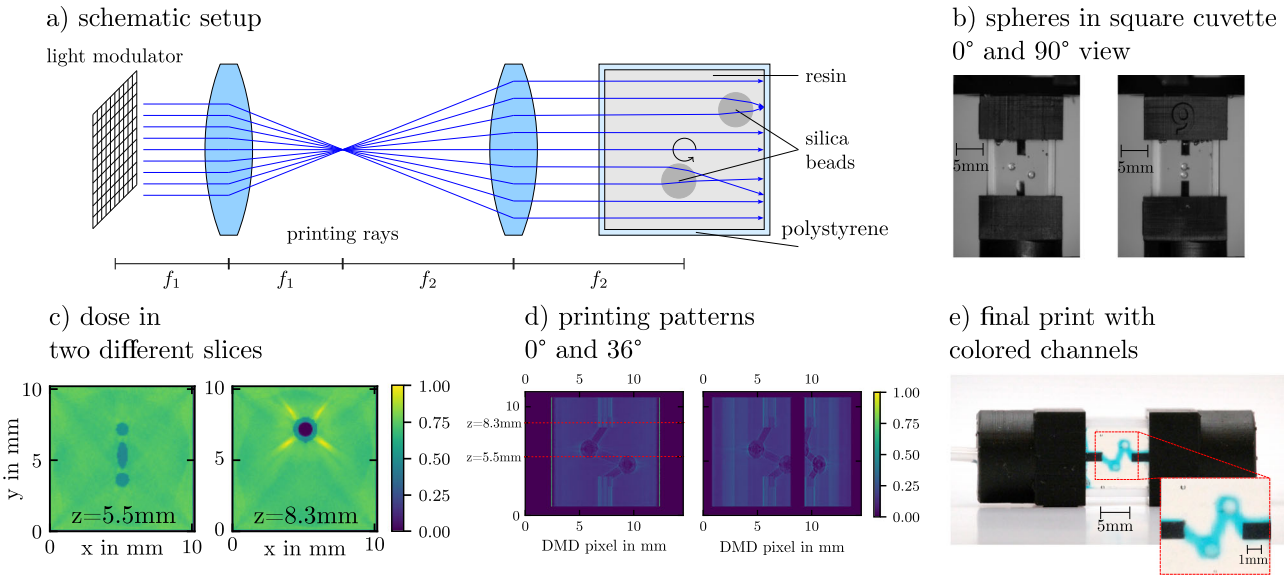



**Fig. 2 | Rapid fabrication of a context-aware microfluidic chip platform.** **a** Schematic setup of the experiment. **b** Images of the spheres embedded in Gel-MA. **c** Cumulative dose distribution across the printing area. **d** Two example projection patterns used for printing. **e** Final print showcasing coloured channels around the embedded spheres.

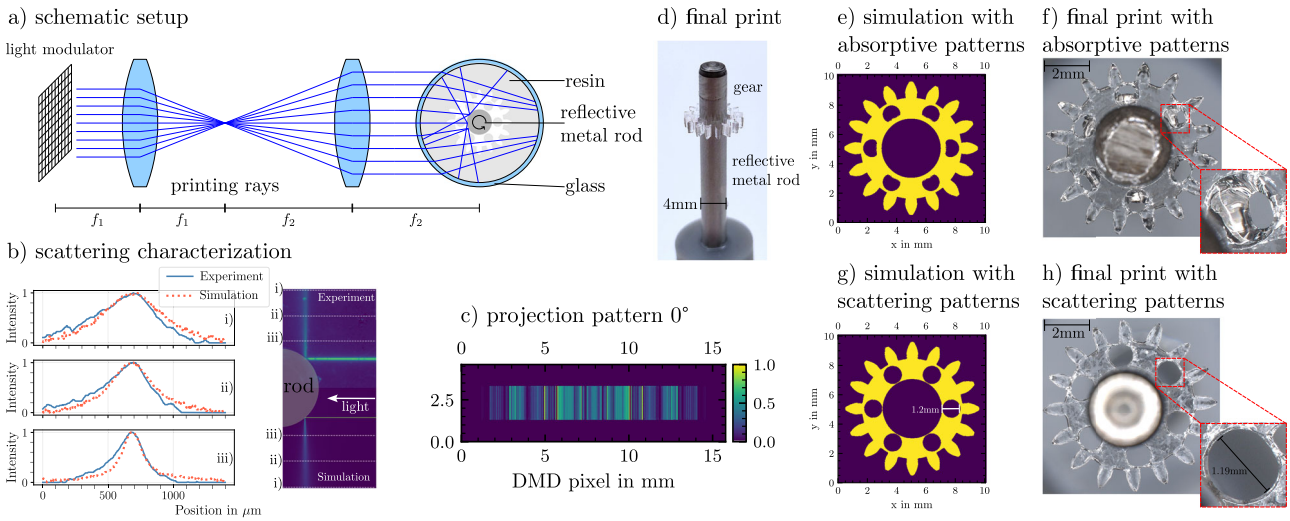



**Fig. 3 | Comparison of printing results assuming an absorptive vs. a reflective rod.** **a** Schematic of the experimental setup. **b** Characterization of scattering behaviour results in $\alpha = 0.03$ used for the Beckmann distribution. **c** An example of an optimized light pattern. **d** The final printed part. **Top row:** Absorptive rod assumption. **e** Simulated print with absorbing patterns projected onto a reflecting rod and **f** final print. **Bottom row:** Scattering rod assumption. **g** Simulated print with scattering patterns projected onto a reflecting rod and **h** final print.

optimized the light patterns for two scenarios. The first assumed a perfectly absorbing rod, as in previous work. The second used a more realistic model of a rough, light-scattering surface. This experiment was performed with LaserTVAM (see Fig. 3a). To characterise the scattering properties of the metal rod, we immersed it into a fluorescent water bath and analyzed the scattered light path from which we can infer a scattering parameter of the Beckmann distribution of $\alpha = 0.03$. The simulated and experimental light paths and three cross-sections are shown in Fig. 3b each. See more details in Section Gear on metal rod.

First, we optimized the patterns for a fully absorbing rod. The final print in the object space after projecting all patterns is displayed in Fig. 3e. The resulting print using these patterns is shown in Fig. 3f. In both the simulation and the experiment, the inner holes of the gear are over-polymerized and incorrectly formed. This result is expected, as these patterns do not account for the light scattered from the metal rod.

In contrast, when we optimize the patterns in Dr.TVAM assuming a reflective metal rod, we achieve better results. One of the optimized patterns is displayed in Fig. 3c. The simulated print in Fig. 3g shows significant improvements over the absorptive case. The gear's holes are well-preserved and by selecting the optimal threshold this optimized projection set reaches a simulated IoU of 0.997 whereas ignoring the scattered light reduces the IoU to 0.942. The final print is shown in Fig. 3d, h. For both scenarios, we conducted a series of experiments with varying exposure levels and selected the print with the highest visual fidelity (see Supplement Exposure series for the experimental results at different power levels). The adhesion of the gear to the rod is relatively high as shown in a demonstration video in the supplementing material (S11). In summary, by accounting for light

https://doi.org/10.1038/s41467-026-73477-3

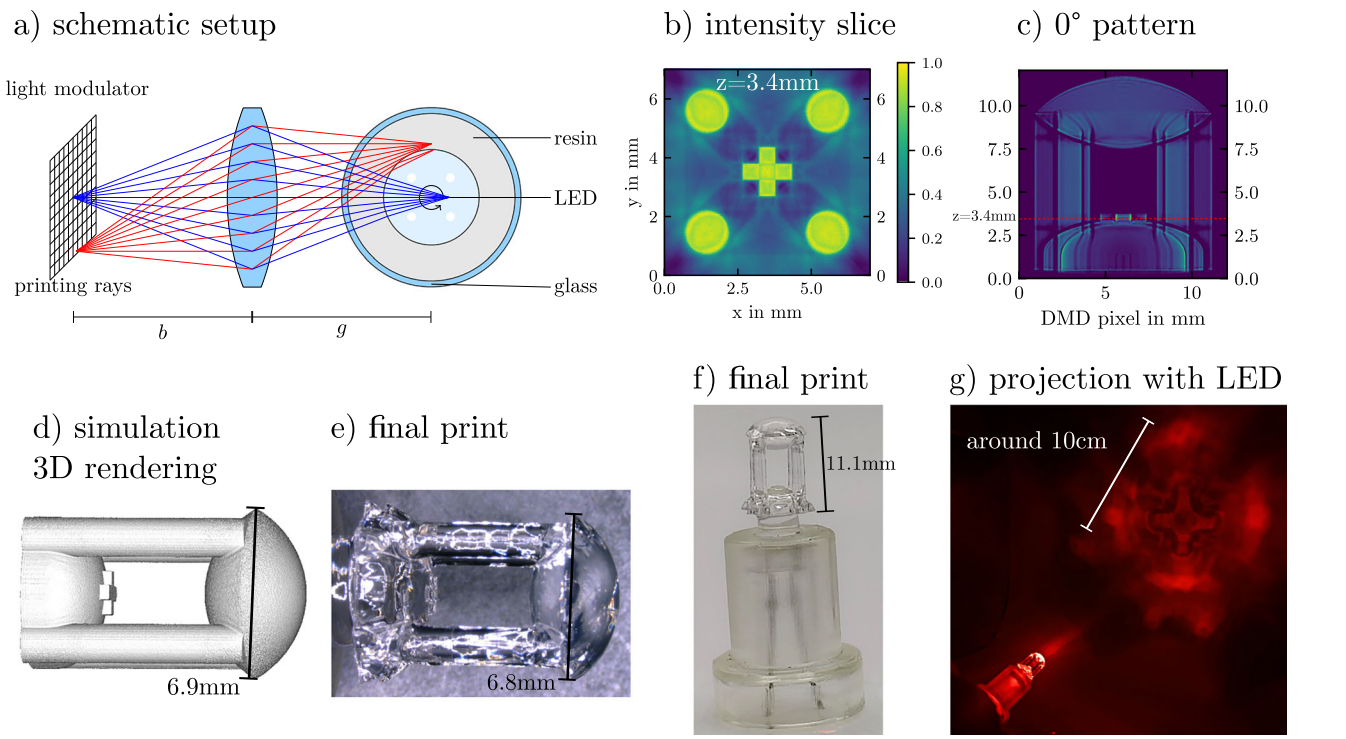



**Fig. 4 | Printing a lens with a symbol directly onto a red LED using LEDTVAM.** **a** Schematic of the general setup. **b** A slice of the dose after projection of all patterns. **c** An example of a single projection pattern. **d** A rendering of the overprinted LED and elements. **e** The final printed lens on the LED. **f** The print on the LED and on the holder. **g** The final image when the overprinted LED is turned on, projecting the ✚ symbol onto a screen.

scattered from the metal rod, Dr.TVAM preserves features close to the rod's surface. In contrast, a model that assumes a fully absorptive rod cannot achieve the same printing fidelity in either simulation or experiment.

### Optical lens with symbol on LED

In this experiment, we print a lens and a lens holder with a symbol directly onto a red LED using an acrylate resin.

To achieve an optically smooth surface, we use a non-telecentric, LED-based TVAM system (LEDTVAM), which is similar to the one described by Webber et al.[18] and detailed in Section LEDTVAM. The light paths in this scenario are complex, involving multiple refractions, reflections, and absorptions at various surfaces and within different media (air, glass, resin, and the LED itself). Our framework, Dr.TVAM, calculates these interactions based on the refractive indices, geometry, and material parameters. The general setup is shown in Fig. 4a, with an LED positioned in the center of the vial. Unlike the collimated rays in the LaserTVAM, each pixel in the LEDTVAM projects a finite cone of light into the resin. Consequently, the resolution of the LEDTVAM is expected to be lower, as its depth of field is dependent on the specific aperture and imaging parameters. Based on Mitsuba, we introduce these non-telecentric setups to Dr.TVAM and make it publicly available.

As shown in Fig. 4b, the optimisation produces a sharp ✚ symbol in the center of the cumulative dose plot. An example of a single projection pattern is shown in Fig. 4c.

The theoretical print is shown in Fig. 4d. The resulting experimental print is shown in Fig. 4e. The lens was printed successfully on top of the LED, and the ✚ symbol is clearly visible on the coating. To place the actual LED inside the resin an SLA-printed cap was press-fit into the vial. The purpose of this lens is to reimage the ✚ symbol; when the LED is turned on, it projects the symbol onto a screen (Fig. 4g).

## Discussion

Dr. TVAM, our open-source framework[13], has the potential to significantly increase the fidelity of light-based additive manufacturing in non-standard optical conditions. By introducing support for a wide variety of overprinting scenarios and enabling both laser-based (LaserTVAM) and LED-based (LEDTVAM) setups, it offers a versatile and accessible solution for diverse applications. Notably, LEDTVAM setups are not possible to simulate with other existing open-source software solutions to this extent.

Here, we demonstrate the capability to directly 3D print inside square perfusable chambers by overprinting around inlets and outlets (Fig. 1). These experiments highlight the potential impact of our framework in biomedical applications. Notably, square vials are particularly advantageous in biofabrication workflows, as their optically flat surfaces make them directly compatible with confocal and light sheet imaging. Furthermore, our overprinting approach enables the direct fabrication of microfluidic biomimetic channels without the need for additional assembly steps, thereby minimising the risk of contamination and mechanical damage. To our knowledge, this is the first time this has been demonstrated with TVAM based methods. There is a similar demonstration by Readily3D SA however it is not a true 3D print and does not overprint occluding inlets.

We also demonstrate that, despite the computational load of our framework, we can still generate a robust set of patterns to dynamically adapt to specific situations, such as arbitrarily positioned spheres within resin Fig. 2. Sphere detection was accomplished using a simple and cost-effective camera system, while pattern calculation was performed on a standard consumer hardware GPU in less than 30 s, all while maintaining a sophisticated optical modeling and optimisation scheme. This strategy enables targeted overprinting of specific structures (e.g., 3D branching networks) upon detection of objects inside the printing chamber (e.g., organoids, spheroids, etc.), thereby enhancing precision and adaptability across a wide range of applications, including but not limited to biofabrication. This approach is

similar to the work by Florczak et al.[24]. However, our method utilises a simpler imaging setup to detect the spheres, and we disclose algorithmic details and source code required for fabrication. Furthermore, our entire pipeline—from object detection and pattern optimisation to the finished print—is completed in less than 3 min.

By accounting for the light scattering surface of a polished metal rod, we have shown through both experimentation and simulation (Fig. 3) that printing fidelity can be improved compared to a simplistic model of a fully light-absorbing rod[1]. TVAM patterns are surprisingly robust against simulation-reality mismatch (such as ignoring scattering) but deviations can become problematic. As presented in our experimental findings, fidelity of fine features located closer to the rod degrades from ignoring those effects and more complex light models (such as ours) are required.

As last example we demonstrated the ability to overprint a symbol and a lens directly onto a small LED. As shown in Fig. 4g, we designed and fabricated an optical system in which any desired pattern can be printed on the LED and projected through a printed lens onto a screen. In this demonstration, we used a ✚ symbol as an example. By incorporating the lens at an appropriate distance from the LED, the system effectively re-images the printed pattern onto the screen, illustrating the potential to integrate arbitrary projection functionalities directly onto compact light sources.

In summary, Dr.TVAM, our computational framework, has shown to be capable of modeling different optical situations for TVAM. As long as the optical material parameters are known, arbitrary scenarios can be assembled and simulated.

With our framework we envision many more overprinting scenarios (such as printing on a reflecting mirror as shown in Supplement Dice on mirror). Since we can model arbitrary shapes and complex material parameters, we are not restricted to the shapes and materials presented here. In fact, the Mitsuba renderer provides a comprehensive library of bidirectional scattering distribution functions (BSDFs), which can be leveraged for accurate modeling of light-surface interactions. We believe this significantly expands the application space for TVAM, enabling the creation of complex, functionalised, and multi-component devices from applications in mechanics, optics or biofabrication.

Nevertheless, opportunities for further enhancement of Dr.TVAM remain, including but not limited to modeling of inhibitor diffusion and optical variations caused by polymerisation-dependent changes of the refractive index during the printing process

# Methods

## Optical setups

**LaserTVAM.** For the laser-based setup, we utilize blue light with a wavelength of $\lambda = 405$ nm (HL40033G, Ushio, Japan), which is coupled into a square multimode optical fiber (WF 70 × 70/115/200/400N, CeramOptec). The projector employed is a high-speed digital micro-mirror device (DMD) (VIS-7001, Vialux), capable of projecting up to 290 Hz of grayscale images. The light from the blue laser diodes is assumed to be homogeneous and square-shaped after exiting the fiber. The measured maximum continuous power of the light source is approximately 450 mW in the printing plane.

To image the DMD, we use a 4f system consisting of two lenses: a 150 mm lens (LA4874-A-ML, Thorlabs) and a 100 mm plano-convex lens. The Fourier stop is employed to filter out higher diffraction orders. For the rotation stage, we utilize a high-precision rotary stage (X-RSW60C, Zaber). The entire setup is synchronised with electrical output signals from the stage, which are wired through an Arduino Nano Every to the DMD.

Within the vial, the light is assumed to be collimated, allowing for the application of parallel ray optics (as shown in Fig. 1a). The depth of field is controlled by the diameter of the aperture. After passing through the 4f system, the DMD pixel size is 20.36 $\mu$m × 20.36 $\mu$m, and the total illuminated area measures 20.849 mm × 15.636 mm for a pattern resolution of 1024 × 768 pixels. The depth of field is around 25 mm assuming a Gaussian beam waist half the pixel size in printing space.

**LEDTVAM.** The LED-based setup utilises a light source with a wavelength of $\lambda = 395$ nm (M395L5, Thorlabs), which has a theoretical maximum power of 1.63 W. This LED is collimated onto a high-speed digital micro-mirror device (DMD) (VIS-7001, Vialux) using a condenser lens. The maximum power in the entire image plane is approximately 80 mW for an active pixel area of 700 × 740 on the DMD. Due to distortions, we opted to not utilize the entire DMD for projections.

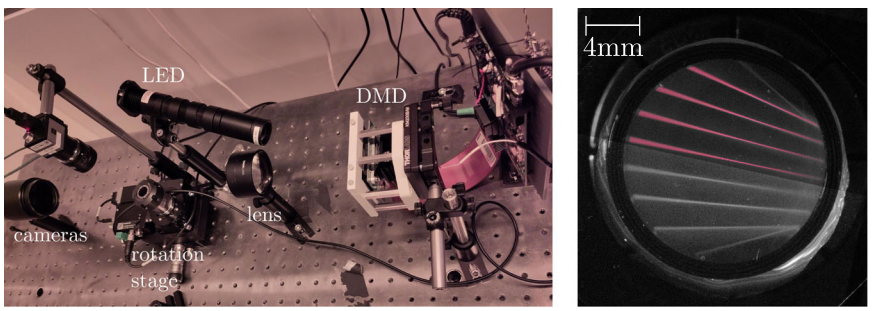
For imaging the DMD, we employed a single 75 mm lens (AC508-075-A-ML, Thorlabs). A high-precision rotary stage (X-RSW60C, Zaber) is used for rotation. The entire setup is synchronised with electrical output signals from the stage, which are routed through an Arduino Nano Every to the DMD.

The general configuration can be observed in Fig. 5a). The LED was roughly collimated onto the DMD, which is imaged by a single lens. Dr.TVAM is capable of modeling such a setup using three parameters: the field of view in the horizontal direction, the aperture, and the distance between the aperture and the focus point.

We made the light paths visible by adding a fluorescence marker to the water. Based on the experimentally measured light paths in a water-filled vial, as illustrated in Fig. 5b, we determined the values of the three parameters. The simulated light path is overlaid in pink. As shown, there is a good match between the experimental results and the simulation.

## Vials

For the overprinting on metal rods, LEDs, and test tubes we used cylindrical glass vials (Fisherbrand 15 14 0548) whose radii are




a) Experimental LEDTVAM setup. b) Measured light path.

**Fig. 5 | Overview of the LEDTVAM setup. a** shows the experimental LEDTVAM setup. **b** shows a top view of the light path in gray. The pink overlay represents the aligned and simulated light path through a water-filled cylindrical glass vial.

$r_{inner}$ = 6.363 ± 0.017 mm and $r_{outer}$ = 7.354 ± 0.016 mm. The refractive index is assumed to be $n$ = 1.54. Adapters to hold the various components in place were designed with CAD software and printed with SLA (Formlabs 3B, Formlabs) using Grey or BioMed black resins (Formlabs). As square vials for the perfusion systems we used 25 mm sections of common spectrophotometer cuvettes ($L_{outer}$ = 12.43 ± 0.03 mm, $L_{inner}$ = 10.07 ± 0.03 mm, $n$ = 1.58) made of polystyrene (7590 30, Brand). Adapters to connect microfluidic tubing and featuring inlet/outlet were designed with CAD software and printed by SLA (Formlabs 3B, Formlabs) using BioMed black resins (Formlabs). We provide access to the design files in Section Code availability.

### Resin preparation

**Acrylate.** As acrylate resins (for Supplement Lenses on test tube and Supplement Dice on mirror) we used di-pentaerythritol pentaacrylate (SR399, Sartomer, France) which was mixed with diphenyl(2,4,6-trimethylbenzoyl)phosphine oxide (TPO, 97%; Sigma-Aldrich) in a planetary mixer (KK-250SE, Kurabo). The refractive index was experimentally determined to be $n$ = 1.4849.

As second resin (for Section Gear on metal rod, Section Optical lens with symbol on LED) we used a mixture of DUDMA (Sigma-Aldrich, USA) and PEGDA 700 (Sigma-Aldrich, USA) in a weight ratio of 4 to 1. The refractive index is $n$ = 1.4840. The concentration of TPO varied between 10 mg and 50 mg per 40 g to 70 g of resin. The printing parameters can be seen in Table 1 and for the pattern optimisation we measured the resulting absorption coefficients as indicated in Table 2. We do not add any inhibitor except oxygen which is naturally dissolved into the resin during mixing.

**Biocompatible resin.** Gelatin-methacryloyl (Gel-MA) was synthesized as previously described[25]. The degree of substitution was calculated using 1H-NMR in D2O using internal standard 3-(trimethylsilyl)-1-propanesulfonic acid (DSS, 2H, ≈ 0.75 ppm), and found to be 0.17 mmol/g. Gel-MA was dissolved at 37° in PBS to result in a 10% (w/v) solution. The photoinitiator lithium phenyl-2,4,6-trimethylbenzoylphosphinate (LAP) was added from a 50× stock solution in PBS to obtain a final concentration of 0.05% (w/v). The resin was then filter sterilized through 0.2 $\mu$m filters. The refractive index was measured to be $n$ = 1.3512.

**Table 1 | Specifications for the pattern optimisation**

| Experiment | $T_{opt}$ in s | $\eta_{energy}$ in % | $T_L$ | $T_U$ | $w_{sparsity}$ |
|---|---|---|---|---|---|
| straight channels | 1166 | 1.5 | 0.6 | 0.9 | 0.02 |
| branched channels | 1175 | 1.5 | 0.6 | 0.9 | 0.02 |
| helix channels | 1182 | 1.4 | 0.6 | 0.9 | 0.02 |
| channels connecting spheres | 19 | 6.1 | 0.6 | 0.9 | 0.0002 |
| absorptive rod | 1460 | 1.6 | 0.7 | 0.92 | 5 |
| reflective rod | 1937 | 1.6 | 0.7 | 0.92 | 5 |
| lens on LED | 4001 | 10.37 | 0.75 | 0.93 | 0.5 |

$T_{opt}$ is the time required for the pattern optimization. $\eta_{energy}$ indicates the energy efficiency of each set of patterns. $T_L$ and $T_U$ are the lower and upper thresholds, respectively, as defined in Equation (1). $w_{sparsity}$ governs the sparsity of the patterns.

### Overprinting experiments

**Perfusion system for bio-applications.** After mounting the square vial in its holder, its angular orientation was aligned (accuracy around ± 0. 5°) by optimizing the back-reflected signal of the printing laser. The resulting calibration was then used to initialize another red reference laser to ensure consistent angular registration. Finally, the vial's vertical position was adjusted under real-time camera observation, enabling precise alignment along the optical axis. We estimate the vertical precision to be around 100 $\mu$m with a camera from behind. The straight channels (Fig. 1g) were designed with a diameter of 0.95 mm. The branched channels (Fig. 1h) featured a main channel width of 0.95 mm that bifurcated into smaller branches of 0.7 mm. The spiral channel (Fig. 1i) and all inlets and outlets maintained a tube diameter of 0.95 mm.

**Context-aware perfusion system.** The square cuvettes were prepared by first filling them with a base layer of warm Gel-MA. The resin was allowed to thermally gel in a refrigerator for 15 min, after which a glass bead with a diameter of 1.0 mm (Thermo Scientific Chemicals) was placed on the gelled surface. This process was repeated by adding a subsequent layer of resin and a second sphere to embed both objects within the hydrogel matrix.

After placing the square vial into the vial holder, we first aligned its angular orientation. Subsequently, we measured the sphere positions from two views (as illustrated in Fig. 2b). This approach enables the determination of the 3D positions in space. Based on these positions, we generated 3D meshes using Python, primarily utilizing `trimesh`, `Gmsh`, and `OpenSCAD`. The generation of the meshes took approximately 10 s. The source code is referenced in Section Code availability.

Using the generated meshes, we then employed Dr.TVAM to optimize the patterns. We utilized only 100 angular projections and reduced the spatial discretization in object space to 10.2 mm/128, which is insufficient to Nyquist sample the resolution of the detector. The optimisation took less than 20 s. However, the generated patterns were adequate to produce satisfactory printing results.

**Gear on metal rod.** The rough surface of the metal rod was modeled using the Beckmann distribution[30]. The Beckmann distribution describes how strong the light is scattered from the rod's surface (see Section Beckmann distribution to model a scattering rod). The rod's geometry, defined by a mesh file, is modulated with a micro-surface

**Table 2 | Experimental conditions for the print**

| Experiment | setup | $P$ in mW/mm$^2$ | $T_{print}$ in s | $\omega$ in °/s | $\mu$ in 1/mm |
|---|---|---|---|---|---|
| straight channels | LaserTVAM | 0.77 | 30.0 | 60.0 | 0.0367 |
| branched channels | LaserTVAM | 0.77 | 30.0 | 60.0 | 0.0367 |
| helix channels | LaserTVAM | 0.77 | 30.6 | 47.0 | 0.0367 |
| channels spheres | LaserTVAM | 0.58 | 19.2 | 60 | 0.0367 |
| absorptive rod | LaserTVAM | 0.30 | 12 | 120 | 0.206 |
| reflective rod | LaserTVAM | 0.33 | 12 | 120 | 0.206 |
| lenses water | LEDTVAM | 0.33 | 30.0 | 60.0 | 0.11 |
| lens LED | LEDTVAM | 0.20 | 25.5 | 113 | 0.197 |

$P$ indicates the maximum power per area available. $T_{print}$ represents the total printing time. $\omega$ denotes the rotational speed of the stage. $\mu$ is the attenuation coefficient used for absorption.

roughness model characterized by the root mean square (RMS) slope. For the metal rod, which had a diameter of 4 mm, the roughness parameter was estimated to be $\alpha$ = 0.03 in Fig. 3b). To obtain the experimental optical trace of the scattered light of a single pixel, we filled a square vial with water and a fluorescent dye. This allows us to make the light path visible. The same scenario was simulated in Dr.TVAM and compared to the experimental results. Lower and higher values of $\alpha$ were tested in Fig. S5 and show less agreement. The rod was precisely positioned in the center of the vial using a custom SLA-printed adapter.

**Optical lens with symbol on LED.** As mentioned, for the last experiment, LEDTVAM was utilized because it produces smooth, striation-free prints, which enables the fabrication of optical components. For the LED overprinting demonstration, commercially available LEDs with a 4.8 mm diameter round cap and a refractive index of ≈ 1.48 were used. Each LED was secured in the center of the printing vial using a custom SLA-printed holder and submerged directly in the resin. The printed lens was designed with a focal length of 4.97 mm, which is sufficient to project the symbol from the LED's surface onto a screen. The radius of curvature of the lens surfaces is 4 mm, the experimental measured radius of curvature is (4.08 ± 0.05 mm).

### Printing and post-processing

**Gel-MA prints.** First, the chip featuring two SLA printed adapters and a polystyrene cuvette section was assembled via press-fitting. Then, silicone microfluidic tubing (OD:4 mm, ID: 0.8 mm) Saint-Gobain) were connected to the barbed adapters on both sides of the chip. Warm (37 °C) Gel-MA photoresin was then injected from one side to fill the chamber. Importantly, the chamber was kept at the right angle to enable evacuation of air bubbles through the venting hole, which was then sealed with a M1 screw. Tubes were then clamped and resin left to thermally crosslink at room temperature for 30 min. After printing, the construct was readily placed in a 37 °C water bath to melt uncrosslinked resin. Warm PBS was then injected via tubing to wash out the channels from residual resin prior to postcuring under UV lamp (Solis-405C, Thorlabs) for 5 s. For better visualization, the perfusable constructs were injected with a blue food dye solution in PBS.

**Acrylate prints.** Acrylate resin was poured into the glass vials and allowed to sit for a few minutes to remove air bubbles. In cases where small, persistent air bubbles remained, the vials were degassed in an ultrasonic bath for 15 min. For various overprinting experiments, the glass vials were equipped with different adapters to accommodate a metal rod, an LED, or a small test tube, as shown in Fig. 3, Fig. 4, and Fig. S1.

After the printing process, the solidified object was placed into a vial containing the solvent propylene glycol monomethyl ether acetate (PGMEA, Sigma-Aldrich). Uncrosslinked resin was washed out by gently shaking the vial with a Reagenzglasschüttler Genie Vortex Mixer Model Vortex-Genie 2 for 10–25 min. The solvent was then replaced with fresh PGMEA, and washing continued for an additional 10–25 min.

Subsequently, the printed part was submerged in PGMEA containing diphenyl(2,4,6-trimethyl-benzoyl)-phosphine oxide (TPO) for 10 min prior to post-curing. The entire vial was then cured under a high-power UV lamp (Solis-405C, Thorlabs) for approximately 1 min. For PEDGA/DUDMA resin we replaced PGMEA with 99% IPA as the viscosity is lower and IPA was sufficient enough for cleaning. After post-curing, the printed construct was placed on a microscopy coverslip and left to air dry.

### Pattern optimization and printing parameters

Table 1 provides details regarding the pattern optimization across various experiments. The gradient-based optimization in Dr.TVAM utilized the following loss function (see also[7,8]):

$$\mathcal{L} = \underbrace{w_{\text{in}} \cdot \sum_{v \in \text{object}} \text{ReLU}(t_u - I_v)^2}_{\text{force polymerization in object}} + \underbrace{w_{\text{out}} \cdot \sum_{v \notin \text{object}} \text{ReLU}(I_v - t_l)^2}_{\text{prevent polymerization elsewhere}} + \underbrace{w_{\text{o}} \cdot \sum_{v \in \text{object}} \text{ReLU}(I_v - 1)^2}_{\text{avoid over-polymerization}} + \underbrace{w_{\text{sparsity}} \cdot \sum_{j \in \text{patterns}} |P_j|^D}_{\text{enforce non-sparse patterns}}. \quad (1)$$

In this equation, $I_v$ represents the absorbed intensity in voxel $v$ after the projection of the patterns. $P_j$ denotes the value of the $j$-th pixel of the patterns. The variables $t_u$ and $t_l$ correspond to the upper and lower thresholds, respectively. The weights $w_{\text{in}}$, $w_{\text{out}}$, $w_{\text{o}}$, and $w_{\text{sparsity}}$ are relative coefficients for the respective terms. The parameter $D$ imposes varying penalties for sparse values.

Some simulation details are summarized in Table 1. An online reference for the complete availability of all configuration files, software, and data is provided in Section Code availability. Most simulations were conducted on a NVIDIA L40S GPU. For the overprinting of the embedded spheres, a desktop computer equipped with a NVIDIA GeForce RTX 4060 Ti was utilized. The spatial discretization and the number of angular patterns for this experiment were significantly reduced, allowing for a substantial decrease in computational time at the expense of quality. Nevertheless, these patterns were adequate to yield satisfactory experimental results.

Furthermore, the energy efficiency of the patterns varies. It is defined as the ratio of the total laser energy transmitted in one rotation to the total energy that would be transmitted if all patterns were fully activated. Dr.TVAM enables control over the sparsity of the patterns; more sparse patterns result in lower energy efficiency. Conversely, less sparse patterns can influence the histogram while still producing high-fidelity prints. In certain cases, we adjust the parameters to optimize the total printing time.

It is important to note that, since the loss function is a summation, the sparsity term is contingent upon the configuration and whether LEDTVAM or LaserTVAM is employed. Consequently, the values presented here are not directly interpretable. We just want to indicate that the sparsity term was utilised to fine-tune the efficiency.

### Experimental printing parameters

Table 2 presents some of the experimental conditions for the prints. To achieve high-quality prints, we varied the power doses by controlling the current supplied to the laser diodes or the LED.

The printing time for all experiments was well below 1 min. Although the number of rotations or the speed was occasionally varied, these factors should not theoretically influence the results. As it can be deduced by their attenuation coefficient $\mu$, for acrylate resins we employed relatively high photoinitiator (TPO) concentrations. In contrast, for the bio-resins, we utilized standard concentrations of the photoinitiator (LAP) commonly used for bioprinting purposes (0.05% w/v).

## Data availability

All raw data generate with Dr.TVAM and the configuration files is available here: https://doi.org/10.5281/zenodo.20038505.

## Code availability

We provide all configuration files for Dr.TVAM and corresponding 3D files for the meshes online to enable reproducibility. Further, we provide access to scripts to generate the context-aware meshes: github.com/EPFL-LAPD/Overprinting-with-Tomographic-Volumetric-Additive-Manufacturing The Zenodo DOI is: https://doi.org/10.5281/zenodo.19187298.

## References


1. Kelly, B. E. et al. Volumetric additive manufacturing via tomographic reconstruction. *Science* **363**, 1075–1079 (2019).
2. Bernal, P. N. et al. Volumetric bioprinting of complex living-tissue constructs within seconds. *Adv. Mater.* **31**, 1904209 (2019).
3. Loterie, D., Delrot, P. & Moser, C. High-resolution tomographic volumetric additive manufacturing. *Nat. Commun.* **11**, 852 (2020).
4. Gibson, I. et al. Vat photopolymerization processes. *Additive manufacturing technologies: 3D printing, rapid prototyping, and direct digital manufacturing*, pp. 63–106 (Springer, New York, 2015).
5. Natterer, F. Inversion of the attenuated radon transform. *Inverse Probl.* **17**, 113 (2001).
6. Rackson, C. M. et al. Object-space optimization of tomographic reconstructions for additive manufacturing. *Addit. Manuf.* **48**, 102367 (2021).
7. Wechsler, F., Gigli, C., Madrid-Wolff, J. & Moser, C. Wave optical model for tomographic volumetric additive manufacturing. *Opt. Express* **32**, 14705–14712 (2024).
8. Wechsler, F., Gigli, C., Madrid-Wolff, J. & Moser, C. SwissVA-MyKnife.jl: An open-source package for tomographic volumetric additive manufacturing. *EPJ Web Conf.* **309**, 03024 (2024).
9. Li, C. C., Toombs, J., Taylor, H. K. & Wallin, T. J. Generalized projection optimization model for tomographic volumetric additive manufacturing. In *Advanced Fabrication Technologies for Micro/Nano Optics and Photonics XVII*, vol. 12898, pp. 82–92 (SPIE, 2024). https://www.spiedigitallibrary.org/conference-proceedings-of-spie/12898/128980E/Generalized-projection-optimization-model-for-tomographic-volumetric-additive-manufacturing/10.1117/12.3008459.full.
10. Loterie, D., Delrot, P. & Moser, C. Method and apparatus for volumetric additive manufacturing with digital distortion compensation (2019). US Patent App. 17/762,834.
11. Orth, A., Sampson, K. L., Ting, K., Boisvert, J. & Paquet, C. Correcting ray distortion in tomographic additive manufacturing. *Opt. Express* **29**, 11037–11054 (2021).
12. Webber, D. et al. Versatile volumetric additive manufacturing with 3d ray tracing. *Opt. Express* **31**, 5531–5546 (2023).
13. Nicolet, B., Wechsler, F., Madrid-Wolff, J., Moser, C. & Jakob, W. Inverse rendering for tomographic volumetric additive manufacturing. *ACM Trans. Graph.* **43**, 228:1–228:17 (2024).
14. Madrid-Wolff, J. et al. A review of materials used in tomographic volumetric additive manufacturing. *MRS Commun.* **13**, 764–785 (2023).
15. Madrid-Wolff, J., Boniface, A., Loterie, D., Delrot, P. & Moser, C. Controlling light in scattering materials for volumetric additive manufacturing. *Adv. Sci.* **9**, 2105144 (2022).
16. Kewitsch, A. S. & Yariv, A. Self-focusing and self-trapping of optical beams upon photopolymerization. *Opt. Lett.* **21**, 24–26 (1996).
17. Rackson, C. M. et al. Latent image volumetric additive manufacturing. *Opt. Lett.* **47**, 1279–1282 (2022).
18. Webber, D. et al. Micro-optics fabrication using blurred tomography. *Optica* **11**, 665–672 (2024). 0 citations (Crossref) [2024-06-27].
19. Weisgraber, T. H. et al. Virtual volumetric additive manufacturing (virtualvam). *Adv. Mater. Technol.* **8**, 2301054 (2023).
20. Orth, A. et al. Deconvolution volumetric additive manufacturing. *Nat. Commun.* **14**, 4412 (2023). 0 citations (Crossref) [2023-08-15].
21. Álvarez Castaño, M. I. et al. Holographic tomographic volumetric additive manufacturing. *Nat. Commun.* **16**, 1551 (2025).
22. Chansoria, P. et al. Synergizing algorithmic design, photoclick chemistry and multi-material volumetric printing for accelerating complex shape engineering. *Adv. Sci.* **10**, 2300912 (2023).
23. Darkes-Burkey, C. & Shepherd, R. F. Volumetric 3d printing of endoskeletal soft robots. *Adv. Mater.* **36**, 2402217 (2024).
24. Florczak, S. et al. Adaptive and context-aware volumetric printing. *Nature* **645**, 108–114 (2025).
25. Sgarminato, V. et al. 3d in vitro modeling of the exocrine pancreatic unit using tomographic volumetric bioprinting. *Biofabrication* **16**, 045034 (2024).
26. Aye, S. S. S., Fang, Z., Wu, M. C. L., Lim, K. S. & Ju, L. A. Integrating microfluidics, hydrogels, and 3d bioprinting for personalized vessel-on-a-chip platforms. *Biomater. Sci.* **13**, 1131–1160 (2025).
27. Rizzo, R. et al. Multiscale hybrid fabrication: volumetric printing meets two-photon ablation. *Adv. Mater. Technol.* **8**, 2201871 (2023).
28. Hasenauer, A. et al. Volumetric printed biomimetic scaffolds support in vitro lactation of human milk-derived mammary epithelial cells. *Sci. Adv.* **11**, eadu5793 (2025).
29. Jakob, W. et al. Mitsuba 3 renderer (2024). https://mitsuba-renderer.org.
30. Beckmann, P. & Spizzichino, A.*The scattering of electromagnetic waves from rough surfaces* (Artech House, Norwood, 1987).


## Acknowledgements

The authors thank Benoît Vignon and Matthieu Borello for their assistance in designing the SLA-printed adapters and Rami Tabbara and the entire Mitsuba team for helpful discussions regarding Dr.TVAM. We are grateful to Ye Pu for designing the lens for the test tube experiment. We also extend our appreciation to Claude Amendola and the mechanical workshop for the precise cutting of the cuvettes. Finally, special thanks to our lab's *pawfessional*, Lucio, for his support during breaks. This project has received funding from the European Research Council (ERC) under the European Union's Horizon 2020 research and innovation program (grant agreement No 948846), and from the Swiss National Science Foundation under project number 196971—*light based volumetric printing in scattering resins*. It also received funding from the Swiss National Science Foundation 2000-1-240074 under grant number 10007068—*Neural precision holographic volumetric additive manufacturing*. R. R. acknowledges Swiss National Science Foundation Return CH Postdoc.Mobility fellowship (P5R5-3_235066).

## Author contributions

F.W.: Conceptualization; Investigation; Experiments; Software; Writing—Original Draft. V.S.: Conceptualization; Investigation; Experiments; Writing—Review & Editing. R.R.: Conceptualization; Investigation; Experiments; Writing—Review & Editing. B.N.: Formal Analysis; Software; Supervision; Writing—Review & Editing. W.J.: Formal Analysis; Supervision; Writing—Review & Editing. C.M.: Formal Analysis; Supervision; Writing—Review & Editing.

## Competing interests

Christophe Moser is a shareholder of Readily3D SA. All the other authors declare no conflict of interest.

## Additional information

**Supplementary information** The online version contains supplementary material available at https://doi.org/10.1038/s41467-026-73477-3.

**Correspondence** and requests for materials should be addressed to Felix Wechsler, Wenzel Jakob or Christophe Moser.

**Peer review information** *Nature Communications* thanks Roozbeh Salajeghe and the other, anonymous, reviewer(s) for their contribution to the peer review of this work. A peer review file is available.

**Reprints and permissions information** is available at http://www.nature.com/reprints

**Publisher's note** Springer Nature remains neutral with regard to jurisdictional claims in published maps and institutional affiliations.

**Open Access** This article is licensed under a Creative Commons Attribution-NonCommercial-NoDerivatives 4.0 International License, which permits any non-commercial use, sharing, distribution and reproduction in any medium or format, as long as you give appropriate credit to the original author(s) and the source, provide a link to the Creative Commons licence, and indicate if you modified the licensed material. You do not have permission under this licence to share adapted material derived from this article or parts of it. The images or other third party material in this article are included in the article's Creative Commons licence, unless indicated otherwise in a credit line to the material. If material is not included in the article's Creative Commons licence and your intended use is not permitted by statutory regulation or exceeds the permitted use, you will need to obtain permission directly from the copyright holder. To view a copy of this licence, visit http://creativecommons.org/licenses/by-nc-nd/4.0/.

© The Author(s) 2026